

Identification of key parameters by comparing experimental and simulated growth of vapor-deposited amorphous $\text{Zr}_{65}\text{Al}_{7.5}\text{Cu}_{27.5}$ films

S. G. Mayr,* M. Moske,† and K. Samwer‡

Institut für Physik, Universität Augsburg, D-86135 Augsburg, Germany

(Received 19 April 1999; revised manuscript received 2 August 1999)

Scanning tunneling microscopy growth studies on vapor-deposited amorphous $\text{Zr}_{65}\text{Al}_{7.5}\text{Cu}_{27.5}$ films are analyzed to identify the dominant surface structure forming mechanisms. Qualitative and—concerning the scaling behavior of surface roughness and height-difference-correlation functions—also quantitative agreement of the experimental results with numerical simulations of a Monte Carlo model and a continuum model can be achieved. Curvature-induced surface diffusion, adatom concentration triggered surface diffusion, and geometrical effects can be identified to be the key parameters for the experimentally observed surface morphology. Some discrepancies, especially in the late stages of growth, remain, but can be explained qualitatively by additional effects, such as tip convolution or by the limitations of the approximations in the model assumptions. [S0163-1829(99)15247-0]

I. INTRODUCTION

The understanding and the modeling of the growth properties of vapor *co*condensed amorphous thin films is of increasing interest—not only due to its technological importance, but also because of its model character for surface growth studies^{1,2}: The absence of a long-range structural order with the lack of lattice constraints and the spatial isotropy enable a simplified quasi-one-dimensional data analysis and description and suggest the possibility of studying the effects of different structure-forming mechanisms,^{3–6} independent from system-specific details concerning the final surface morphology. Particularly, due to the lack of well-defined steps, in amorphous systems the Ehrlich-Schwoebel barrier^{7–9}—which is dominant in many crystalline systems in forming mesalike structures—is not known to be present, which offers the possibility of investigating other mechanisms independently. In this sense amorphous films can be deemed to supplement the universal aspects of the numerous experimental and theoretical studies published in the last decade.^{1,2} In addition, the surface morphology is tightly linked to film stresses, which have been the topic of earlier investigations.¹⁰

For modeling on an atomic scale, molecular dynamics and kinetic Monte Carlo simulations, as well as, in the continuum limit, Langevin-type rate equations for the surface $h(\vec{x}, t)$; $\vec{x} = (x, y)$ of the form

$$\frac{\partial h(\vec{x}, t)}{\partial t} = F[h(\vec{x}, t)] + \eta(\vec{x}, t) + I(\vec{x}, t) \quad (1)$$

are successfully applied to account for significant features of film growth.¹ Here, $F[h(\vec{x}, t)]$ denotes a functional, containing the different surface processes, and $\eta(\vec{x}, t)$ is a spatial and temporal uncorrelated Gaussian noise, as a fluctuation of the mean particle flux I , which is independent of \vec{x} and t for homogeneous and continuous deposition, i.e.,

$$\langle \eta(\vec{x}, t) \rangle_{\text{ensemble}} = 0, \quad (2)$$

$$\langle \eta(\vec{x}, t) \eta(\vec{x}', t') \rangle_{\text{ensemble}} = 2D \delta(\vec{x} - \vec{x}') \delta(t - t'). \quad (3)$$

The flux term I can be set $\equiv 0$ by the choice of a comoving coordinate system. For a quantitative characterization of surface morphologies, the rms roughness σ , the height-difference-correlation function $H(r)$,^{11,12} and the radially averaged spectral power density $C(q)$ (Ref. 13)

$$\sigma(L, t) = \sqrt{\langle h(\vec{x}, t)^2 \rangle_{\vec{x}}} \quad (4)$$

(where L is the image size),

$$H(r) = \langle [h(\vec{R}) - h(\vec{x} + \vec{R})]^2 \rangle_{\vec{R}, |\vec{x}|=r} \quad (5)$$

can be applied [$\langle h(\vec{x}, t) \rangle_{\vec{x}} = 0$]. In the case of a self-affine surface growth, these quantities show a characteristic scaling behavior in dependence of their parameters, e.g., in the case of $H(r)$ the roughness exponent 2α , and the dynamical exponent β for $\sigma(t)$.

In this paper we present, beginning from STM growth studies, a Monte Carlo and continuum model, which is then numerically solved. A comparison of all approaches allows us to identify the main structure-forming mechanisms in amorphous film growth.

II. EXPERIMENTAL DETAILS

The glassy $\text{Zr}_{65}\text{Al}_{7.5}\text{Cu}_{27.5}$ films^{14,15} are *co*condensed onto thermally oxidized Si wafers (thickness of the thermal oxide SiO_2 diffusion barrier: 500 nm) by three independently rate-controlled electron beam evaporators under ultrahigh vacuum conditions in a three-chamber UHV system (base pressure: 2×10^{-10} mbar) using a total evaporation rate of 0.79 nm/sec. Prior to deposition, the wafers are heat cleaned for at least an hour, using a temperature of at least 360 K. The surface roughness of the wafers was determined by small-angle x-ray diffraction and a fit with a spectrum simulation¹⁶ to be (0.3 ± 0.1) nm. During deposition, the substrate is rotated with typically 40 rpm to ensure a homogeneous film composition and thickness. The geometrical arrangement of the substrate and crucibles guarantees a particle flux normal to the substrate within 5° . The heat coupling of the substrate to the bath is good enough to limit a tempera-

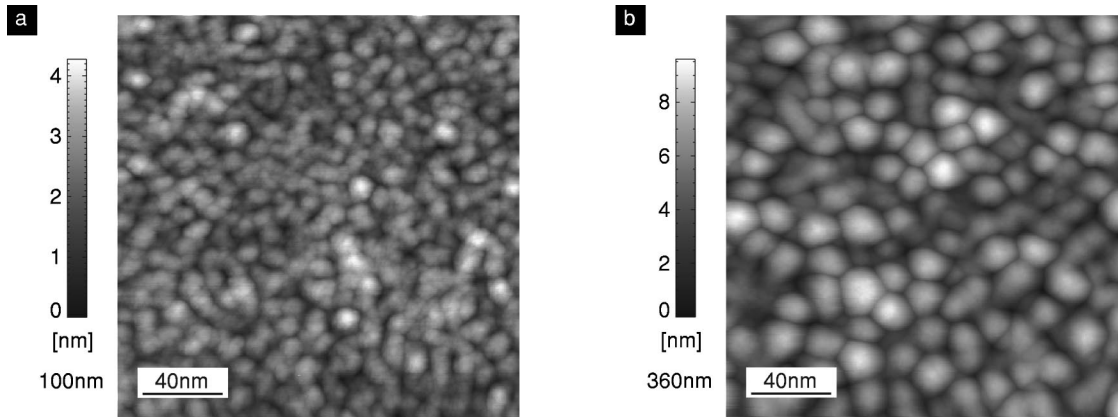


FIG. 1. Surface topographs of a 100-nm-thick (a) and a 360-nm-thick (b) $Zr_{65}Al_{7.5}Cu_{27.5}$ film deposited at room temperature onto SiO_2 at a constant rate of 0.79 nm/sec recorded with STM using comparable scanning parameters: the lateral size and the height of the mesoscopic hill-like structures increase with increasing film thickness.

ture rise from the beginning of film deposition to film completion to less than 10 K. After transfer, the films are investigated *in situ* using Auger electron spectroscopy (for film composition control and possible surface contamination) and by STM (Omicron STM 1) using electrochemically etched tungsten tips in constant current mode (typical scanning parameters: $U_T \approx 1.0V$; $I_T \approx 1.0nA$). The amorphicity is verified *ex situ* with x-ray diffraction and partially by differential scanning calorimetry (DSC) measurements. Further details can be found in earlier works.^{17,18}

III. EXPERIMENTAL RESULTS

Figure 1 shows two images from a film thickness series evaporated at room temperature. More detailed images—especially concerning the early stages of film growth—have already been presented elsewhere.^{3,4} The growth can be characterized by the initial formation of mesoscopic hill-like structures, which grow with increasing film thickness in the lateral size R_C and hill height (characterized by the root-mean-square roughness σ) until a saturation of both values occurs [saturation values: $R_C = (19 \pm 0.5)$ nm, $\sigma = (1.7 \pm 0.3)$ nm] in the range of a film thickness of 200 nm (the errors refer to the results from numerous repetitions of the experiment).^{3,18} While the saturation of the rms roughness has to be interpreted carefully due to the measurement method applied (convolution of the STM tip with the surface

morphology, i.e., the tip might not be able to reach the valley bottoms in some areas because of the finite tip angle), the behavior of the lateral growth saturation is unambiguous. The final morphologies can be shown to be independent from the details of the substrate, as shown in Fig. 2, where two films prepared on SiO_2 and relaxed $Zr_{65}Al_{7.5}Cu_{27.5}$, respectively, (prepared at higher temperature) are shown. No major difference is seen. This means that the surface morphology is independent of the initial conditions on a wide range and depends mainly on the deposition parameters and the material system (for instance, an increase of Cu content at the expense of Al leads to smoother surfaces, Figs. 3 and 4). The roughness exponent $\alpha = 0.8 \pm 0.1$ and dynamical exponent $\beta = 0.2 \pm 0.1$ have already been determined in earlier investigations.^{3,18} In addition, all STM topographs discussed here show—when measured with sufficient resolution—further structures on an atomic scale, which can be attributed to exposed surface atoms or clusters of atoms in an amorphous state.⁴

In the following, the mechanisms for the pronounced structure formation and high lateral correlations on the surface are identified with the help of two kinds of computer models: A Monte Carlo and a continuum model.

IV. MONTE CARLO MODEL

Monte Carlo simulations of film growth have to use a crystal lattice, which underlies the atomic processes,¹⁹ and

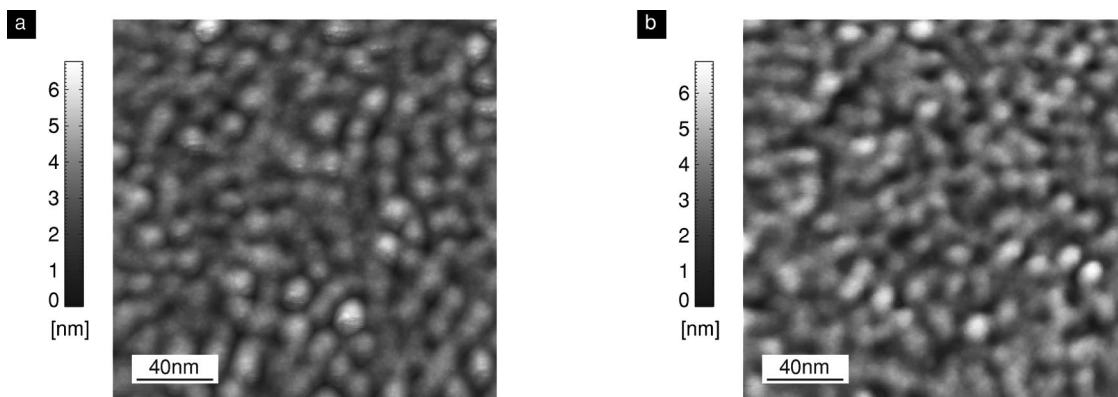


FIG. 2. $Zr_{65}Al_{7.5}Cu_{27.5}$ films (200 nm) on two different substrates: (a) prepared on SiO_2 and (b) prepared on relaxed $Zr_{65}Al_{7.5}Cu_{27.5}$.

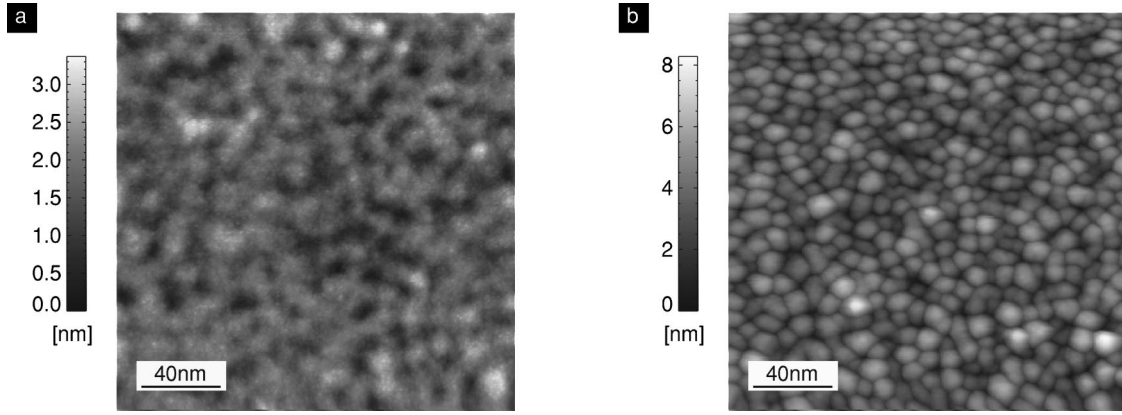


FIG. 3. Dependence of the surface morphology on the film composition for 100-nm-thick films, recorded with STM: with decreasing Cu content [from (a) to (b)], the lateral size of the mesoscopic hills decreases, and the roughness increases.

therefore omit the consideration of a truly amorphous structure. From a mesoscopic point of view, however, amorphous and crystalline films (independent of the details of the lattice) generally behave quite similarly, if comparable microscopic processes and spatial isotropy are present. In this sense, Monte Carlo models are predestinated to study the effect of single atomic processes on the mesoscopic morphology: Single atoms are deposited ballistically normal to the surface, where they immediately relax—this incorporation mechanism (“hot atoms effect”) mimics local heat pulses due to the acceleration of the atoms towards the surface, which has been proven to lead to local relaxation.²⁰ Consecutively, surface diffusion acts in smoothing, where the jump probability is weighted with the jump distance to ensure isotropy. Volume effects and desorption are neglected due to the much slower kinetics. To speed up the simulation, a clustering effect (i.e., the ceasing of all kinetics, if the binding energy exceeds a threshold of ten atoms), and a maximum number of diffusional jumps (1000 steps) serve as a cutoff for diffusion. Although realistic values for the parameters (i.e., the binding energy per atom $W=0.4$ eV, the “attempt-frequency” for diffusion $\omega_{\text{Debye}}=1 \times 10^{13}$ Hz and substrate temperature $T_{\text{substrate}}=300$ K) are applied, the results only claim correctness on a qualitative level due to the simplifications discussed above, and concentrate on the behavior of large amounts of atoms in amorphous systems, rather than simulational details. Additionally, the effect of the STM measurement itself via tip convolution (a cone-shaped tip, tip angle = 40°) is optionally included, where with tip simulation the roughness is reduced. Figure 5 shows topographs from two different stages of film growth. Both the lateral structures as well as the roughness saturate with the film thickness, as shown in Fig. 6. A roughness exponent of $\alpha=0.8 \pm 0.1$, and a dynamical exponent $\beta=0.2 \pm 0.1$ can be determined.

V. MODELING WITH CONTINUUM EQUATIONS

The experimentally determined decay of the radially averaged spectral power density $C(q)$ with a power law of q^{-4} (frequency q) and the Monte Carlo (MC) results suggest curvature-induced surface diffusion (according to Mullins) as one dominant surface relaxation process,^{3–6} considered for the one-dimensional surface $h(x)$: The gradient of the

chemical potential μ , which is set proportional to the local curvature $1/r$,

$$\mu \propto -\frac{1}{r} = -\frac{\frac{\partial^2 h}{\partial x^2}}{\left[1 + \left(\frac{\partial h}{\partial x}\right)^2\right]^{3/2}} \quad (6)$$

is the driving force for a diffusional current and leads—together with the assumption of mass conservation, as desorption is neglected (for substrate temperatures ≤ 650 K, a supersaturation of the vapor of 10^{10} or greater is estimated)—to the following equation (D_S is a constant proportional to the surface diffusion constant):

$$F_D[h] = -D_S \frac{\partial}{\partial x} \left\{ \left[1 + \left(\frac{\partial h}{\partial x} \right)^2 \right]^{-1/2} \frac{\partial}{\partial x} \left(\frac{1}{r} \right) \right\}. \quad (7)$$

Additionally, the observed coarsening with increasing film thickness can be attributed to a diffusion current driven by a concentration gradient of the adatoms due to the different slopes of the surface, as has been shown by Moske:²¹ Re-

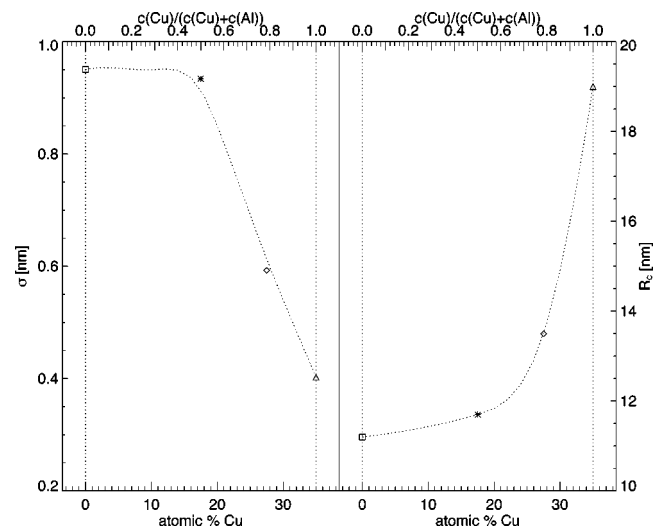


FIG. 4. Dependence of the surface roughness σ and lateral size R_C of the mesoscopic hills on the Cu content—film thickness: 100 nm.

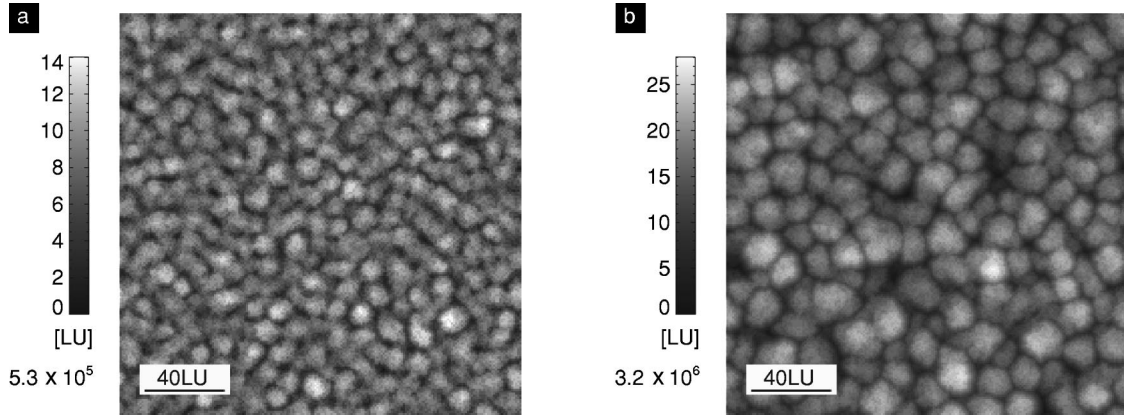


FIG. 5. Two topographs for the early (a) and late (b) stages, created by the Monte Carlo model (with tip simulation). The number of deposited particles is given at the margin of the images (LU: length unit).

gions with high slope retrieve a lower net flux of atoms perpendicular to the local surface than regions parallel to the substrate (the total particle beam is assumed to be normal to the substrate), and thus reveal a lower adatom density c , $c_0 = \text{const}$:

$$c = c_0 \left[1 + \left(\frac{\partial h}{\partial x} \right)^2 \right]^{-1/2}. \quad (8)$$

This leads to concentration-gradient-triggered diffusion [the expression for $\mu \propto -1/r$ in Eq. (7) is replaced by c]. This effect is also implicitly present in the MC simulations by the isotropic relaxations of atoms immediately after atom deposition ($C = \text{const}$):

$$F_C[h] = C \frac{\partial}{\partial x} \left\{ \left[1 + \left(\frac{\partial h}{\partial x} \right)^2 \right]^{-1/2} \frac{\partial}{\partial x} \left[1 + \left(\frac{\partial h}{\partial x} \right)^2 \right]^{-1/2} \right\}. \quad (9)$$

A further microscopic effect, especially for amorphous systems, may be attributed to the finite size and attraction perpendicular to the surface of the atoms, leading to antidiffusional behavior,^{22,23} as protrusions from the surface are favored in comparison to grooves concerning particle deposition, analogous to the ballistic deposition mechanism in the MC model,²⁴

$$F_S[h] = -S \frac{1}{r} = -S \frac{\frac{\partial^2 h}{\partial x^2}}{\left[1 + \left(\frac{\partial h}{\partial x} \right)^2 \right]^{3/2}}. \quad (10)$$

Thus the total equation considered for the deposition process then assumes the form

$$\frac{\partial h}{\partial t} = F_D[h] + F_C[h] + F_S[h] + \eta. \quad (11)$$

Except for the coarsening term [Eq. (9)], this equation is similar to the one considered by Golubovic and Karunasiri.²⁵ Linearization of Eq. (11) for small spatial derivatives, neglecting all terms of order 3 and higher, leads to the following expression:

$$\frac{\partial h}{\partial t} = -D_S \frac{\partial^4 h}{\partial x^4} - \frac{C}{2} \frac{\partial^2}{\partial x^2} \left(\frac{\partial h}{\partial x} \right)^2 - S \frac{\partial^2 h}{\partial x^2} + \eta, \quad (12)$$

with the most unstable mode¹³ for, e.g., $C=0$, $D_S > 0$, $S > 0$ at $q = \sqrt{S/2D_S}$, growing exponentially for short times in the nonstochastic case.²³

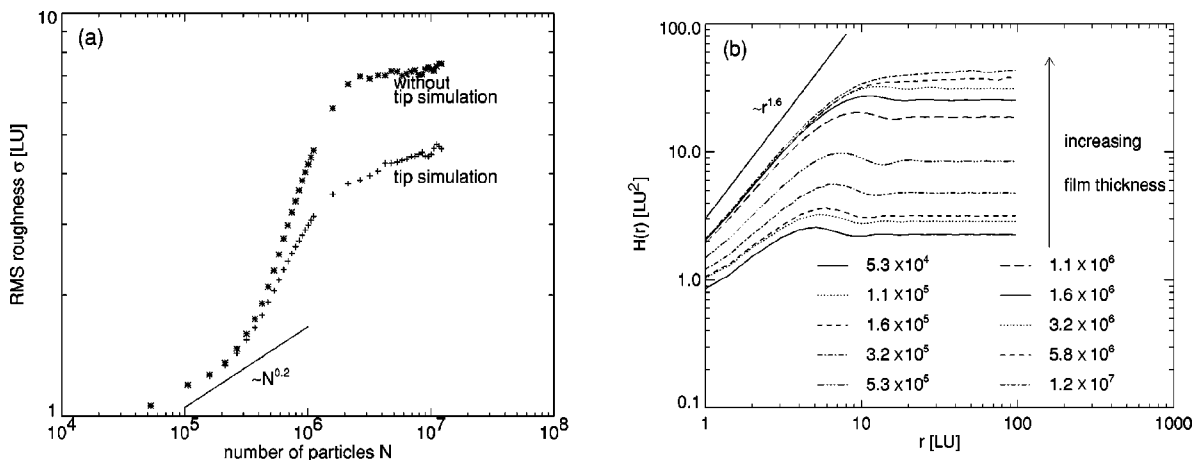


FIG. 6. RMS roughness σ versus the number of deposited particles (a), and height-difference correlation functions for various film thicknesses (b): The roughness shows a pronounced increase in the medium range; in the early stages it grows much slower with film thickness ($\beta = 0.2 \pm 0.1$), and in the late stages it saturates. $\alpha = 0.8 \pm 0.1$ can be determined from $H(r)$.

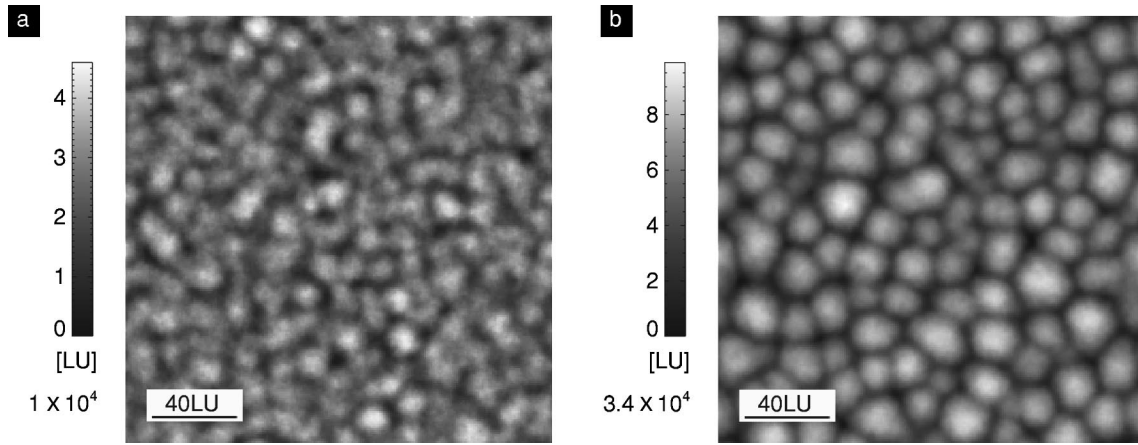


FIG. 7. Topographs generated by numerical integration (Euler method) of the continuum model on a 200×200 grid, $\Delta t = 0.001$, $\Delta x = 0.7$, $D = 0.1$, $D_S = 2$, $C = 5$, $S = 1$ in units of Δx and Δt . The numbers at the margin denote the integration steps (proportional to the deposition time and film thickness).

In order to test the validity of the suggested model, a comparison of the experimental and simulation results in three dimensions is desirable, which incorporates the metric tensor. However, in the linearized regime, this can be achieved by replacing $\partial/\partial x$ by $\nabla_{xy} = (\partial/\partial x, \partial/\partial y)$. The discretization in space is performed by the standard finite difference scheme,^{26,28} and the Euler and Heun method^{27,28} in time, leading to similar results. The coefficients are varied for good accordance with the experiments: Starting from stability considerations as discussed above, the most unstable wavelength, which should dominate the STM topographs in the early times, is given by the ratio of D_S and S . The individual parameters according to this ratio are then chosen with regard to the other parameters, especially C , for an optimum agreement with the experiments. A different method for parameter estimation will be discussed elsewhere.²⁹ Figure 7 shows two images of the simulation from different stages of film growth, and the appropriate roughness values and correlation functions are depicted in Fig. 8. Characteristic hill-like structures, which show an increase of the lateral hill size and hill height with film thickness, can be observed. The film roughness follows a power law of $t^{0.2}$ in the early stages, where the increase with the film thickness slows

down in the late stages with a maximum slope in the medium range. The height-difference correlation functions show a scaling behavior similar to the experiments. It should be emphasized that only with such sets of parameters, within a limited range, and within a possible rescaling between coefficients and time, it was possible to reproduce the experimentally observed structure formation. Especially, all terms considered prove to be necessary: The coefficients D_S together with S are responsible for the growth instability experimentally observed and determine the characteristic structure size in the early stages. C is responsible for the structure coarsening, the slowing down of the growth of the unstable modes, and the generation of the asymmetry between $+h$ and $-h$, predominantly visible in the STM measurements. An increase (decrease) of C around the values selected for the numerical investigation leads to an increased (decreased) tendency for the structures to coarsen.

VI. COMPARISON OF EXPERIMENTS AND SIMULATIONS

Both experimental results and the simulations show qualitatively comparable surface structures that evolve similarly

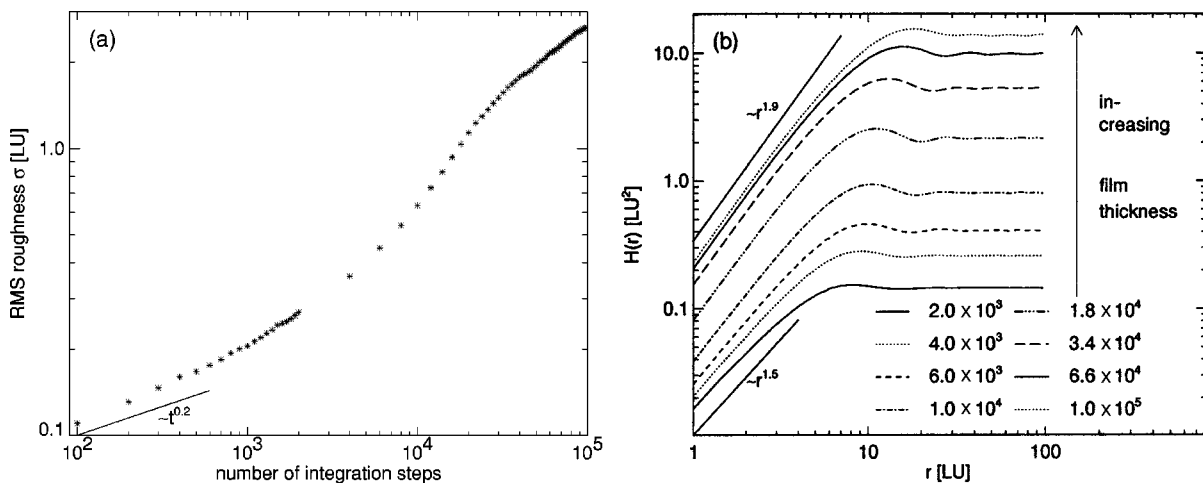


FIG. 8. RMS roughnesses σ (a) and height-difference correlation functions $H(r)$ (b) for various stages of simulated film growth using the continuum model (time unit: number of integration steps): A scaling exponent $\beta = 0.2 \pm 0.1$ and $\alpha = 0.85 \pm 0.15$ can be determined.

with time, i.e., show coarsening. However, the mesoscopic hill-like structures in the continuum model in the late stages have deeper grooves in between, and the slowing down of the lateral size R_C and roughness σ —if present in the experiments (see above)—cannot be determined unambiguously here, whereas it is obvious in the Monte Carlo simulation (see Fig. 6). Experimentally, the saturation of the roughness with increasing film thickness in the late stages is enhanced by the tip convolution, which can be understood as an effect, where the tip is unable to reach the surface of the valleys between two hills due to geometrical reasons. Both numerical methods show a surface roughness, which, at the beginning of film growth, increases much slower with thickness than in the medium stages, see Figs. 6 and 8. At the beginning the dynamical exponents are in accordance with the experimental results within the error bars. Also the roughness exponents show values comparable with the experiments. The remaining discrepancies, especially in comparison to the continuum model, might be attributed to the fact, that in experiments additional influences, such as the finite incidence angle of the particles, shadowing effects, volume effects, or the STM measuring artifact due to the tip geometry might occur. Vice versa the assumptions made in modeling, especially the small gradient approximation, remain no longer valid in the late stages of film growth.²⁴ However, the results strongly suggest that curvature-induced surface diffusion, a concentration-gradient-driven diffusion, and geometrical effects together can be positively identified to be responsible for the main features in amorphous film growth.

VII. CONCLUSION

The identification of the growth mechanisms together with the experimental knowledge of their parameter dependence, as described in this paper, suggest the possibility of tailoring film surface properties for technical needs: By an increase of the deposition temperature, and thus the diffusion coefficient, the coefficients of curvature-induced diffusion as well as for adatom-triggered diffusion can be expected to increase, and thus the typical structure size, as well as the coarsening tendency will grow (constant deposition rate presupposed), with the effect of generating smoother films, as desirable in most applications. A similar effect can be achieved by the appropriate choice of a film component with a higher surface diffusion coefficient (see the experiments with a variation of the Cu content) or a decrease of S and D [which defines the noise intensity—see Eq. (3)] via a reduced deposition rate. It is noteworthy that for glasses with an enhanced region of undercooled liquid, e.g., $Zr_{65}Al_{7.5}Cu_{27.5}$, an annealing treatment can also be a method to achieve the desired surface topography.³

ACKNOWLEDGMENTS

The authors acknowledge fruitful discussions with B. Reinker, especially concerning his experience with the STM and image processing, and the technical support of A. Spörhase with the UHV–thin-film preparation. This work was supported by the DFG Sonderforschungsbereich 438 München–Augsburg, TP A1, Germany.

*Electronic address: Stefan.Mayr@Physik.Uni-Augsburg.DE

[†]Present address: Research Center caesar, Friedensplatz 16, D-53111 Bonn, Germany.

[‡]Present address: I. Physikalisches Institut, Universität Göttingen, Bunsenstr. 9, D-37073 Göttingen, Germany.

¹A. L. Barabasi and H. E. Stanley, *Fractal Concepts in Surface Growth* (Cambridge University Press, Cambridge, 1995).

²M. Marsili, A. Maritan, F. Toigo, and J. R. Banavar, *Rev. Mod. Phys.* **68**, 963 (1996).

³B. Reinker, M. Moske, and K. Samwer, *Phys. Rev. B* **56**, 9887 (1997).

⁴S. G. Mayr, M. Moske, and K. Samwer, *Europhys. Lett.* **44**, 465 (1998).

⁵W. W. Mullins, *J. Appl. Phys.* **28**, 333 (1957).

⁶W. W. Mullins, *J. Appl. Phys.* **30**, 77 (1959).

⁷R. L. Schwoebel and E. J. Shipsey, *J. Appl. Phys.* **37**, 3628 (1966).

⁸G. Ehrlich and F. G. Hudda, *J. Chem. Phys.* **44**, 1039 (1966).

⁹Stefan G. Mayr, Maggie E. Taylor, Harry A. Atwater, Michael Moske, and Konrad Samwer *Appl. Phys. Lett.* (to be published).

¹⁰M. Moske and K. Samwer, *Z. Phys. B: Condens. Matter* **77**, 3 (1988).

¹¹G. Rasigni, F. Varnier, M. Rasigni, J. P. Palmari, and A. Llebaria, *Phys. Rev. B* **27**, 819 (1983).

¹²S. K. Sinha, E. B. Sirota, S. Garoff, and H. Stanley, *Phys. Rev. B* **38**, 2297 (1988).

¹³W. M. Tong and R. S. Williams, *Annu. Rev. Phys. Chem.* **45**, 401 (1994).

¹⁴A. Inoue, T. Zhang, and T. Masumoto, *Mater. Sci. Eng., A* **134**, 1125 (1991).

¹⁵A. Inoue, T. Zhang, and T. Masumoto, *J. Non-Cryst. Solids* **150**, 396 (1992).

¹⁶H. Geisler, Ph.D. dissertation, Wißner-Verlag, Augsburg, 1996 (Wißner-Verlag, Augsburg, 1997).

¹⁷B. Reinker, Ph.D. dissertation, Wißner-Verlag, Augsburg, 1996 (Wißner-Verlag, Augsburg, 1997).

¹⁸S. G. Mayr, Diploma thesis, Augsburg, 1997 (unpublished).

¹⁹E.g., P. A. Maksym, *Semicond. Sci. Technol.* **3**, 594 (1988).

²⁰G. De Lorenzi and G. Ehrlich, *Surf. Sci. Lett.* **293**, L900 (1993).

²¹M. Moske, Habilitation thesis, Augsburg, 1997.

²²N. J. Shevchik, *J. Non-Cryst. Solids* **12**, 141 (1973).

²³A. Mazor, D. J. Srolovitz, P. S. Hagan, and B. G. Bukiet, *Phys. Rev. Lett.* **60**, 424 (1988).

²⁴P. Koblinski, A. Maritan, F. Toigo, R. Messier, and J. R. Banavar, *Phys. Rev. E* **53**, 759 (1996).

²⁵L. Golubovic and R. P. U. Karunasiri, *Phys. Rev. Lett.* **66**, 3156 (1991).

²⁶W. H. Press, B. P. Flannery, S. A. Teukolsky, and W. T. Vetterling, *Numerical Recipes in Pascal* (Cambridge University Press, Cambridge, 1989).

²⁷P. E. Kloeden, E. Platen, H. Schurz, *Numerical Solution of SDE through Computer Experiments* (Springer-Verlag, Berlin, 1991).

²⁸J. G. Amar and F. Family, *Phys. Rev. A* **41**, 3399 (1990).

²⁹M. Raible, S. G. Mayr, S. J. Linz, M. Moske, P. Hänggi, and K. Samwer (unpublished).